Short Papers

Analysis of Low-Loss Broadside-Coupled Dielectric Image Guide Using the Mode-Matching Technique

BHARATHI BHAT, SENIOR MEMBER, IEEE, AND ANUP K. TIWARI, STUDENT MEMBER, IEEE

Abstract—**The solutions of electromagnetic field equations of the broadside-coupled dielectric image guide are derived using the mode-matching technique. The even- and odd-mode dispersion characteristics are presented as a function of the dimensional parameters of the guide for the low-loss mode for which the principal electric field is parallel to the metal image planes.**

I. Introduction

The use of dielectric integrated circuits at millimeter-wave frequencies has received increased attention in recent years [1]–[10]. The transmission losses in the dielectric guides used as the basic transmission media in these circuits are reasonably small. However, the radiation loss at the curved sections of these guides, except in the case of the trapped image guide [8] and the nonradiative dielectric guide [10], often exceeds the tolerance limit. In the trapped image guide, the metallic trough reduces the radiation loss by redirecting the energy leaking from the bends back to the dielectric portion of the guide. However, the metallic trough makes the structure bulky and rather impractical for integrated circuit applications. The nonradiative dielectric guide proposed by Yoneyama and Nishida [10] is supported between two parallel metallic plates with the plate separation being less than half a wavelength. This guide is reported to have negligible radiation loss at the curved sections. Introducing an air-gap at the center of the dielectric slab parallel to the metallic plates results in a broadside-coupled dielectric guide as shown in Fig. 1. This structure can be regarded as a special case of the broadside-coupled dielectric image line, where the principal electric field is parallel to the metal image plane.

In the case of a single dielectric image line, Shindo and Itanami [11] have shown that the transmission loss for the mode having the principle electric field parallel to the metal image plane is nearly less than half of the conventional mode having the electric field perpendicular to the image plane. Broadside-coupled image lines, when excited with the electric field parallel to the image planes, should therefore find potential applications in the design of low-loss millimeter-wave components, especially couplers and filters. The analysis of such broadside-coupled structures is not reported so far.

In this paper, we apply the mode-matching technique [12], [13] to determine the general electromagnetic field solutions of broadside-coupled dielectric image lines. Detailed data are generated on the even- and odd-mode propagation constants as a function of the structural parameters for the excitation having the principal E-field component parallel to the image planes.

Manuscript received April 26, 1983; revised February 3, 1984. This work was supported by the Research and Training Scheme of the Defence Research and Development Organization of the Ministry of Defence, India.

The authors are with the Centre for Applied Research in Electronics, Department of Electrical Engineering, Indian Institute of Technology, Hauz Khas, New Delhi-110016, India.

II. Analysis

Fig. 1 shows the cross section of a broadside-coupled dielectric guide with a rectangular shielding enclosure. The metallic side walls at $x=-a$ and $(3a+2s)$ serve as image planes for the guiding structure. The top and bottom conductors are separated by a distance $(2p+b)$ and the height p can be chosen sufficiently large so that these conductors have negligible effect on the electromagnetic fields of the coupled dielectric guide.

Due to the symmetry of the structure with respect to the plane PP', the analysis can be carried out in terms of the even and odd modes. At the plane PP', a magnetic wall can be assumed for the even modes and an electric wall for the odd modes. It is then sufficient to consider only one-half of the structure as shown in Fig. 2, for the purpose of analysis. We assume the wave propagation to be in the z direction, and the field components to vary as $e^{-j\beta z}$, where β is the propagation constant in the z direction. To facilitate the calculation of electromagnetic fields in the transverse plane, the field region is divided into four parts as shown in Fig. 2. In such a structure, fields in any direction may be taken as a combination of TM and TE fields in that direction [14]. The electromagnetic fields of these modes can be expressed in terms of two scalar potentials f_m^e and f_n^h which are proportional to the E_y and H_y field components

$$E_{ym}=\frac{1}{\epsilon_r}\left(\beta^2-\frac{\partial^2}{\partial x^2}\right)f_m^e(x,y) \tag{1}$$

$$H_{yn}=\left(\beta^2-\frac{\partial^2}{\partial x^2}\right)f_n^h(x,y) \tag{2}$$

where ϵ_r is the relative dielectric constant of the region under consideration. In this paper, we approximate the hybrid fields in terms of TM mode to y (TM^y) and TE mode to y (TE^y). For the TM^y mode, the electromagnetic fields are expressed in terms of only f_m^e by setting $f_n^h=0$, and for the TE^y mode, the fields are expressed in terms of only f_n^h by setting $f_m^e=0$. The potential functions in the four regions marked 1 to 4 in Fig. 2 for the TM and TE modes are given by the following:

Region 1: $(-a\leqslant x\leqslant a, \quad p+b\leqslant y\leqslant 2p+b)$:

$$f_{1m}^e(x,y)=\sum_{m=1}^{M}\left\{B_m\cos(\beta_{1xm}x)+B_m'\sin(\beta_{1xm}x)\right\}\cdot\cos\left[\beta_{1ym}\{y-(2p+b)\}\right] \tag{3}$$

$$f_{1n}^h(x,y)=\sum_{n=1}^{N}\left\{G_n\cos(\bar{\beta}_{1xn}x)+G_n'\sin(\bar{\beta}_{1xn}x)\right\}\cdot\sin\left[\bar{\beta}_{1yn}\{y-(2p+b)\}\right]. \tag{4}$$

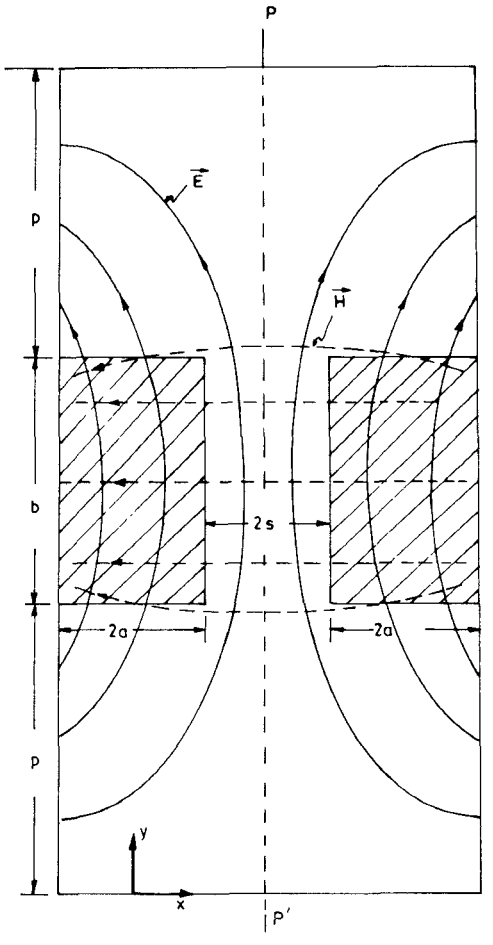

Fig. 1 Cross-sectional view of the broad side-coupled dielectric image guide and its typical field lines

Region 2: $(-a \leqslant x \leqslant a, \quad p \leqslant y \leqslant p+b)$:

$$f^e_{2m}(x,y) = \sum_{m=1}^{M} \{C_m \cos(\beta_{2xm}x) + C'_m \sin(\beta_{2xm}x)\} \cdot [F_m \cos\{\beta_{2ym}(y-p)\} + F'_m \sin\{\beta_{2ym}(y-p)\}] \quad (5)$$

$$f^h_{2n}(x,y) = \sum_{n=1}^{N} \{H_n \cos(\bar{\beta}_{2xn}x) + H'_n \sin(\bar{\beta}_{2xn}x)\} \cdot [K_n \cos\{\bar{\beta}_{2yn}(y-p)\} + K'_n \sin\{\bar{\beta}_{2yn}(y-p)\}]. \quad (6)$$

Region 3: $(-a \leqslant x \leqslant a, \quad 0 \leqslant y \leqslant p)$:

$$f^e_{3m}(x,y) = \sum_{m=1}^{M} [\{D_m \cos(\beta_{3xm}x) + D'_m \sin(\beta_{3xm}x)\} \cdot \cos(\beta_{3ym}y)] \quad (7)$$

$$f^h_{3n}(x,y) = \sum_{n=1}^{N} [\{J_n \cos(\bar{\beta}_{3xn}x) + J'_n \sin(\bar{\beta}_{3xn}x)\} \cdot \sin(\bar{\beta}_{3yn}y)]. \quad (8)$$

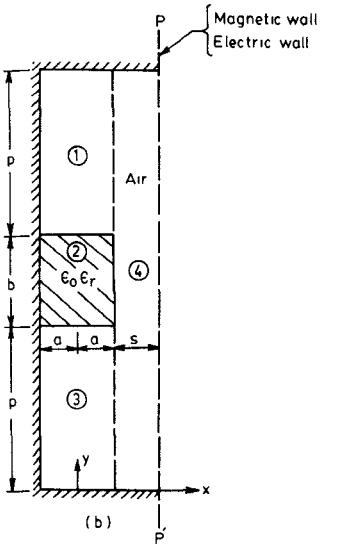

Fig. 2. Cross-sectional half-portion of the broadside-coupled dielectric image guide for calculation of field distribution.

Region 4: $(a \leqslant x \leqslant a+s, \quad 0 \leqslant y \leqslant 2p+b)$:

For a magnetic wall at $x = (s+a)$:

$$f^e_{4m}(x,y) = \sum_{m=0}^{M} E_m \cos\{\beta_{4xm}(x-s-a)\} \cos(\beta_{4ym}y) \quad (9)$$

$$f^h_{4n}(x,y) = \sum_{n=0}^{N} L_n \sin\{\bar{\beta}_{4xn}(x-s-a)\} \sin(\bar{\beta}_{4yn}y). \quad (10)$$

For an electric wall at $x = (s+a)$:

$$f^e_{4m}(x,y) = \sum_{m=0}^{M} E_m \sin\{\beta_{4xm}(x-s-a)\} \cos(\beta_{4ym}y) \quad (11)$$

$$f^h_{4n}(x,y) = \sum_{n=0}^{N} L_n \cos\{\bar{\beta}_{4xn}(x-s-a)\} \sin(\bar{\beta}_{4yn}y). \quad (12)$$

In the above equations, β_{1xm}, β_{2xm}, β_{3xm}, and β_{4xm} are the wave numbers in the x-direction of the TM^y modes, and $\bar{\beta}_{1xn}$, $\bar{\beta}_{2xn}$, $\bar{\beta}_{3xn}$, and $\bar{\beta}_{4xn}$ are those of the TE^y modes. When the subscript x is replaced by y, these symbols denote the wavenumbers of TM^y and TE^y modes in the y direction. The various wave numbers are related by the following equations:

$$\begin{aligned} \beta_0^2 &= \beta_{1xm}^2 + \beta_{1ym}^2 + \beta^2 = \bar{\beta}_{1xn}^2 + \bar{\beta}_{1yn}^2 + \beta^2 \\ \epsilon_r\beta_0^2 &= \beta_{2xm}^2 + \beta_{2ym}^2 + \beta^2 = \bar{\beta}_{2xn}^2 + \bar{\beta}_{2yn}^2 + \beta^2 \\ \beta_0^2 &= \beta_{3xm}^2 + \beta_{3ym}^2 + \beta^2 = \bar{\beta}_{3xn}^2 + \bar{\beta}_{3yn}^2 + \beta^2 \\ \beta_0^2 &= \beta_{4xm}^2 + \beta_{4ym}^2 + \beta^2 = \bar{\beta}_{4xn}^2 + \bar{\beta}_{4yn}^2 + \beta^2 \end{aligned} \quad (13)$$

where β_0 is the free-space propagation constant. We now set the tangential electric-field components equal to zero at the conducting boundaries $y = 0$ and $y = 2p + b$ and also at $x = -a$. Further, matching the tangential electric and magnetic fields at the interface $y = p$ between the regions 2 and 3 and also at $y = p + b$ between the regions 1 and 2, we obtain

$$\beta_{4ym} = \frac{m\pi}{2p+b}, \qquad m = 0,1,2,\cdots \quad (14)$$

$$\bar{\beta}_{4yn} = \frac{n\pi}{2p+b}, \qquad n = 1,2,3,\cdots \tag{15}$$

$$\beta_{1xm} = \beta_{2xm} = \beta_{3xm} = \beta_{xm} \tag{16}$$

$$\bar{\beta}_{1xn} = \bar{\beta}_{2xn} = \bar{\beta}_{3xn} = \bar{\beta}_{xn} \tag{17}$$

$$\frac{B_m}{B'_m} = \frac{C_m}{C'_m} = \frac{D_m}{D'_m} = \tan(\beta_{xm}a) \tag{18}$$

$$\frac{G_n}{G'_n} = \frac{H_n}{H'_n} = \frac{J_n}{J'_n} = -\cot(\bar{\beta}_{xn}a) \tag{19}$$

$$\beta_{1ym}\tan(\beta_{1ym}p) + \frac{\beta_{2ym}}{\epsilon_r}\tan(\beta_{2ym}b) + \beta_{3ym}\tan(\beta_{3ym}p) = \left\{(\epsilon_r\beta_{1ym}\beta_{3ym})/\beta_{2ym}\right\}\tan(\beta_{1ym}p) \cdot \tan(\beta_{2ym}b)\tan(\beta_{3ym}p) \tag{20}$$

$$\frac{\bar{\beta}_{3yn}}{\bar{\beta}_{2yn}} = \tan(\bar{\beta}_{1yn}p) + \frac{\bar{\beta}_{1yn}}{\bar{\beta}_{2yn}}\tan(\bar{\beta}_{3yn}p) + \frac{\bar{\beta}_{3yn}\bar{\beta}_{1yn}}{\bar{\beta}^2_{2yn}}\tan(\bar{\beta}_{2yn}b) = \tan(\bar{\beta}_{2yn}b)\tan(\bar{\beta}_{3yn}p)\tan(\bar{\beta}_{1yn}p). \tag{21}$$

Matching the tangential field components E_y, E_z, and H_z at $x = a$ over the range $0 \leqslant y \leqslant p$, $p \leqslant y \leqslant p+b$, and $p+b \leqslant y \leqslant 2p+b$, and by solving, taking into account an equal number of TM^y and TE^y modes ($M = N$), we obtain the following equations:

TM^y Modes:

Even mode:

$$\alpha_t(\beta^2 + \beta^2_{4xt})E_t^{(1)} = \sum_{m=1}^{M}(\beta^2 + \beta^2_{xm})B_m^{(1)}W_m, \qquad t = 0,1,2,\cdots,M-1 \tag{22}$$

$$j\beta E_t^{(2)} = \sum_{m=1}^{M} j\beta B_m^{(1)}Z_m, \qquad t = 1,2,\cdots,M-1 \tag{23}$$

$$\alpha_t j\omega\epsilon_o E_t^{(3)} = \sum_{m=1}^{M} j\omega\epsilon_o\beta_{xm}B_m^{(2)}W_m^{(1)}, \qquad t = 0,1,2,\cdots,M-1. \tag{24}$$

Odd mode:

$$\alpha_t\left\{-(\beta^2 + \beta^2_{4xt})\right\}E_t^{(4)} = \sum_{m=1}^{M}(\beta^2 + \beta^2_{xm})B_m^{(1)}W_m, \qquad t = 0,1,2,\cdots,M-1 \tag{25}$$

$$-j\beta E_t^{(5)} = \sum_{m=1}^{M} j\beta B_m^{(1)}Z_m, \qquad t = 1,2,3,\cdots,M-1 \tag{26}$$

$$\alpha_t j\omega\epsilon_o E_t^{(6)} = \sum_{m=1}^{M} j\omega\epsilon_o\beta_{xm}B_m^{(2)}W_m, \qquad t = 0,1,2,\cdots,M-1. \tag{27}$$

TE^y Modes:

Even mode:

$$\alpha_t\{-j\omega\mu_o\}L_t^{(1)} = \sum_{n=1}^{M} j\omega\mu_o\bar{\beta}_{xn}G_n^{(1)}\overline{W}_n, \qquad t = 0,1,2,\cdots,M-1 \tag{28}$$

$$-j\beta L_t^{(3)} = \sum_{m=1}^{M} j\beta G_n^{(2)}\overline{Z}_n, \qquad t = 1,2,3,\cdots,M-1 \tag{29}$$

$$\alpha_t\{-\beta^2 + \beta^2_{4xt}\}L_t^{(2)} = \sum_{n=1}^{M}(\beta^2 + \bar{\beta}^2_{xn})G_n^{(2)}\overline{W}_n, \qquad t = 0,1,2,\cdots,M-1 \tag{30}$$

Odd mode:

$$\alpha_t\{-j\omega\mu_o\}L_t^{(4)} = \sum_{n=1}^{M} j\omega\mu_o\bar{\beta}_{xn}G_n^{(1)}\overline{W}_n, \qquad t = 0,1,2,\cdots,M-1 \tag{31}$$

$$j\beta L_t^{(6)} = \sum_{n=1}^{M} j\beta G_n^{(2)}\overline{Z}_n, \qquad t = 1,2,\cdots,M-1 \tag{32}$$

$$\alpha_t(\beta^2 + \beta^2_{4xt})L_t^{(5)} = \sum_{n=1}^{M}(\beta^2 + \bar{\beta}^2_{xn})G_n^{(2)}\overline{W}_n, \qquad t = 0,1,2,\cdots,M-1 \tag{33}$$

where the expressions for the various parameters appearing in (22)–(33) are given in the Appendix.

From the above set of equations, β can be computed by varying its value from 0 to $\beta_o\sqrt{\epsilon_r}$ and finding its zero crossing for TM^y and TE^y modes separately. In this paper, we shall present numerical results only for the TM^y (E^y_{pq}) modes of the guide. The results of the nonradiative dielectric waveguide reported by Yoneyama and Nishida [10] can be obtained as a special case by setting s = 0.

III. Numerical Results

Fig. 3 shows a typical plot of the normalized propagation constant β/β_o as a function of p/b at two frequencies, namely, 25 and 35 GHz. It is apparent from this graph that the top and bottom metal conductors have negligible effect on β/β_o for $p/b \geqslant 2$ when β/β_o is greater than 1. Hence in all the subsequent computations, p/b is assumed to be 2.

The variation of β/β_o as a function of frequency for the E^y_{11} and E^y_{21} even- and odd-modes (denoted as E^y_{11e}, E^y_{11o}, E^y_{21e} and E^y_{21o}) of the broadside-coupled dielectric guide are plotted in Figs. 4, 5, and 6 for the aspect ratios $b/2a = 5/3$, 1, and 3/5, respectively. The half spacing s between the dielectric strips is the variable parameter. The dielectric chosen in all three cases is polystyrene having $\epsilon_r = 2.56$. It is observed from Figs. 4–6 that in the case of an even-coupled mode, the dispersion curves for various spacings $2s$ between the dielectric strips cross each other at $\beta/\beta_o = 1$, whereas, for the odd mode, they do not cross. Further, for $\beta/\beta_o > 1$, the even- and odd-mode propagation constants approach each other with increasing value of s. This phenomenon may be explained as follows. The region $\beta/\beta_o < 1$ corresponds to the waveguide modes, while the region $\beta/\beta_o > 1$

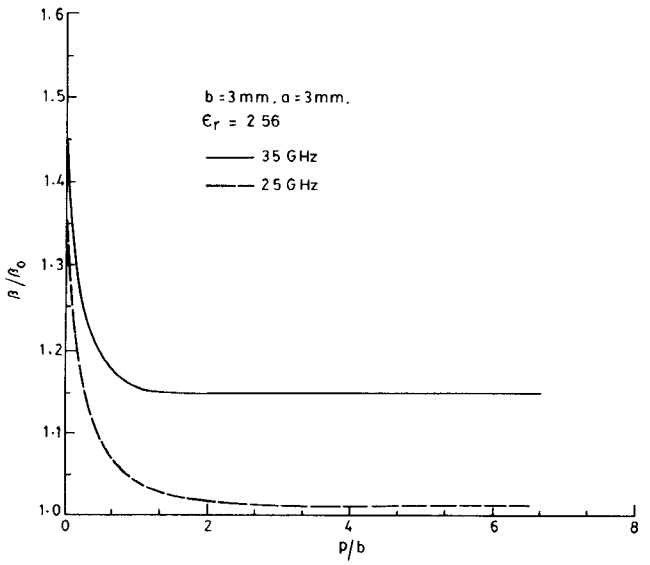

Fig. 3. Normalized propagation constant β/β_o versus p/b of the dielectric image guide for E_{11}^y mode ($s \to \infty$ in Fig. 2).

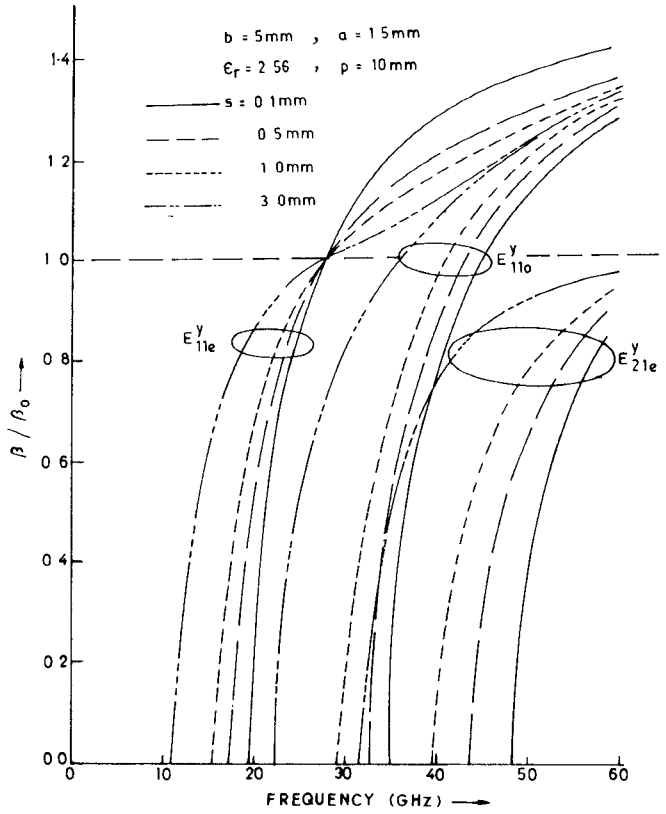

Fig. 4. Normalized propagation constant β/β_o versus frequency of the broadside-coupled dielectric image guide with polystyrene dielectric and aspect ratio 5/3.

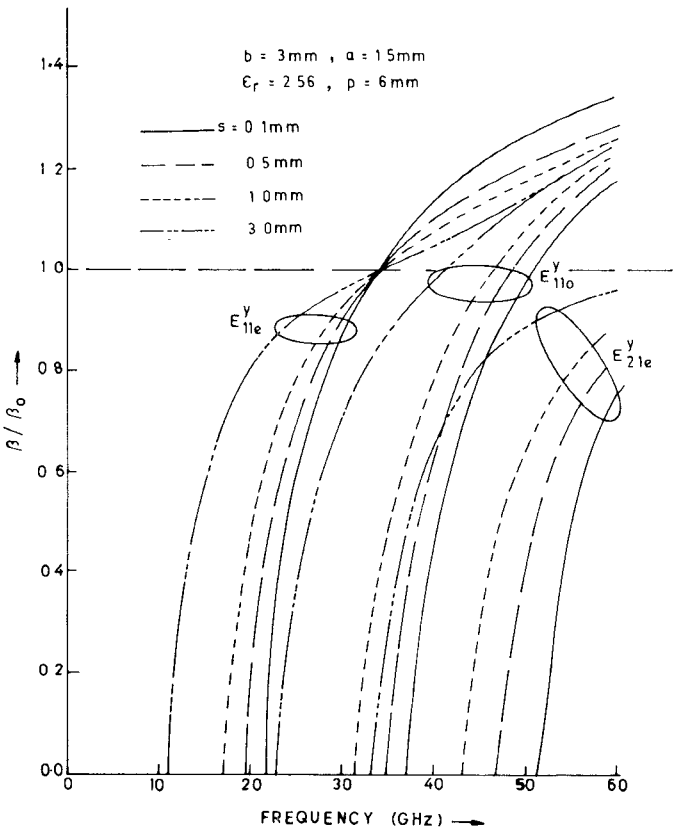

Fig. 5. Normalized propagation constant β/β_o versus frequency of the broadside-coupled dielectric image with polystyrene dielectric and aspect ratio 1.

corresponds to the dielectric image guide modes. Further, for $\beta/\beta_o > 1$, the fields in region 4 are evanescent. The coupling between the two dielectric strips decreases with an increase in s and for sufficiently large values of s, the even-mode propagation constant becomes equal to the odd-mode propagation constant.

For the parameters chosen in Figs. 4–6, the odd-mode cutoff frequencies are greater than the cutoff frequency of parallel plate structures having a plate separation equal to $2(2a+s)$ and, hence, the structure is not "nonradiative." Fig. 7 shows the variation of β/β_o with frequency for a larger value of $\epsilon_r = 9.6$ and a higher aspect ratio $b/2a = 3/2$. With these parameters, the structure is nonradiative.

Fig. 8 shows the variation of effective coupling length as a function of frequency for 3-dB, as well as 0-dB coupling for various values of half-spacing s between the two coupled dielectric strips. The aspect ratio chosen is 3/5 and the dielectric constant of the strips is 2.56. The effective length is calculated as given by Rudokas and Itoh [6]. Referring to Fig. 8, the ratio of the power between the ports 2 and 3 is given by

$$\frac{P_3}{P_2} = \tan^2\left(\frac{\pi l}{2L}\right)$$

$$L = \frac{\pi}{\beta_{ze} + \beta_{zo}}$$

$$l' = l + \frac{\Delta\phi}{\pi} \cdot L$$

$$\Delta\phi = \int_{zo}^{z'} [\beta_{ze}(z) - \beta_{zo}(z)]\, dz$$

where

l' effective length of the coupler,
l length of coupled guide,
β_{ze} even-mode propagation constant,
β_{zo} odd-mode propagation constant.

For the same values of aspect ratio and ϵ_r, the variation of coupling length with frequency for 3- and 0-dB couplings in the case of a side-coupled conventional image guide has been plotted in the same figure. It can be seen from Fig. 8, that, for a fixed set

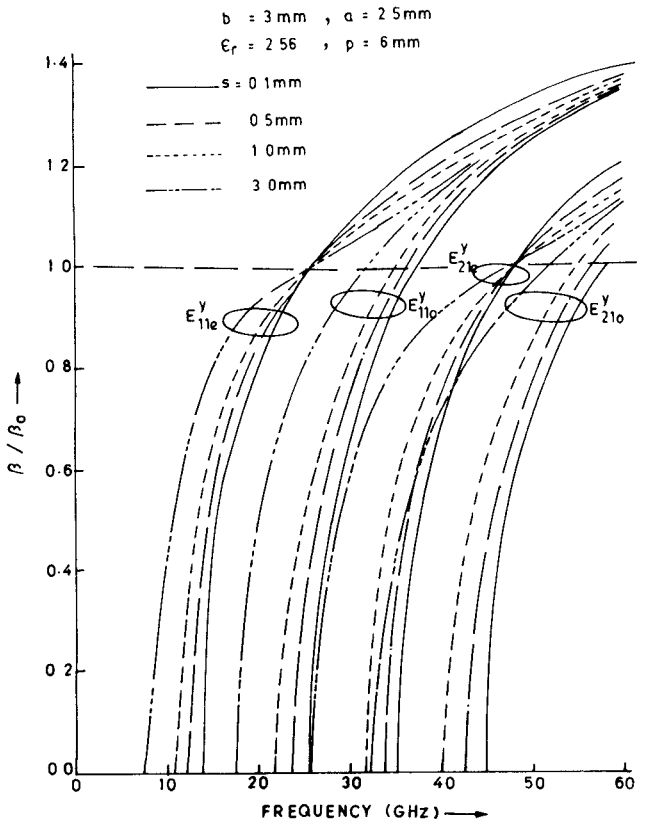

Fig. 6. Normalized propagation constant β/β_o versus frequency of the broadside-coupled dielectric image guide with polystyrene dielectric and aspect ratio 3/5.

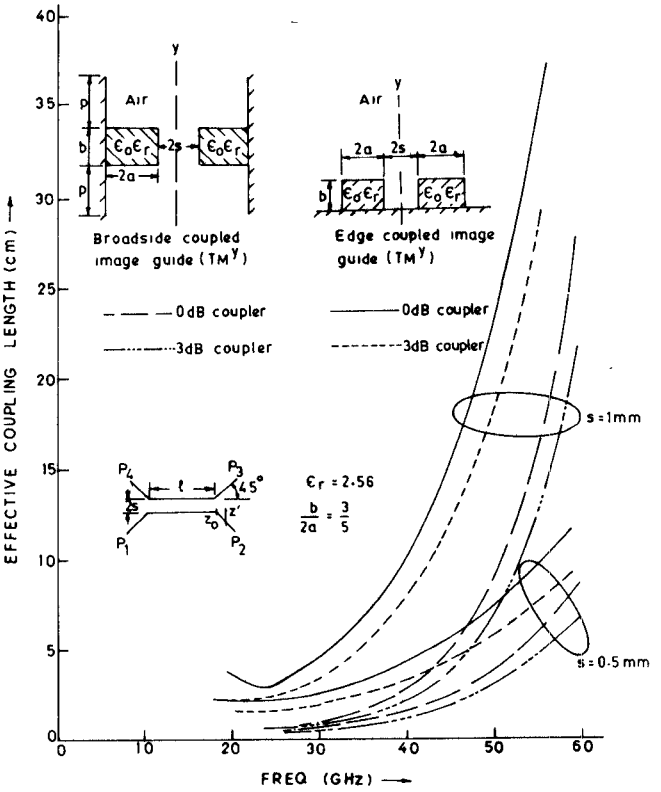

Fig. 8. Effective coupling length versus frequency of 3- and 0-dB broadside-coupled couplers and side-coupled couplers using polystyrene dielectric.

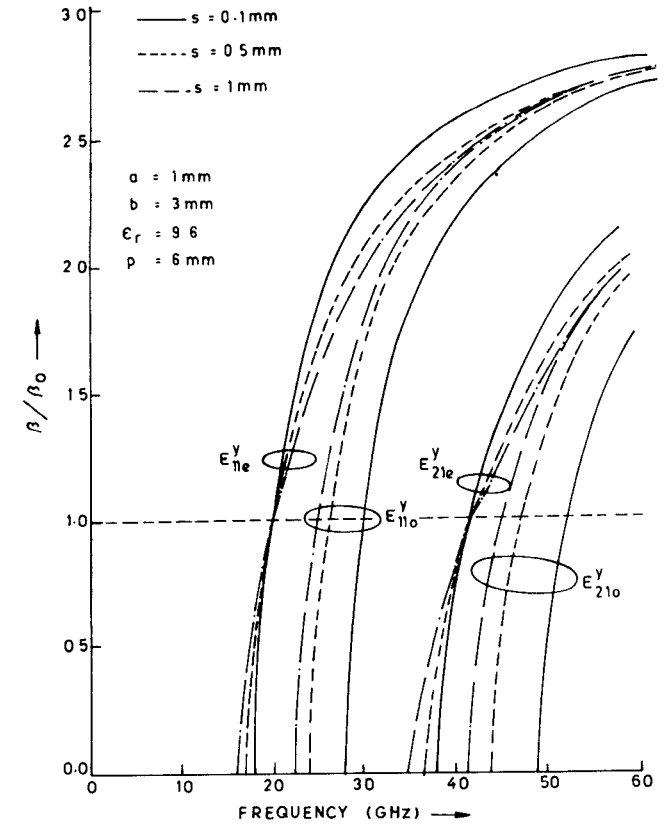

Fig. 7. Normalized propagation constant β/β_o versus frequency of the broadside-coupled dielectric image guide with alumina dielectric and aspect ratio 3/2.

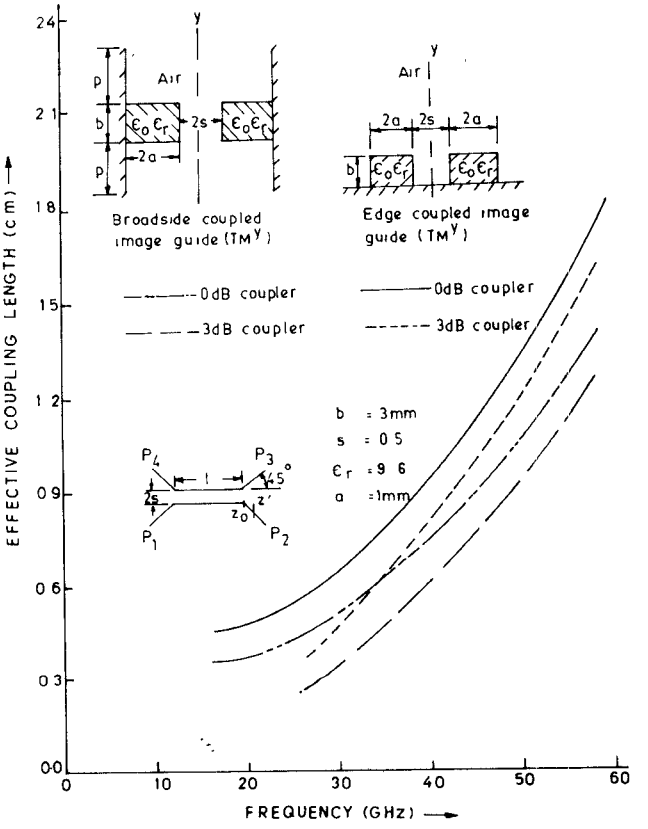

Fig 9. Effective coupling length versus frequency of 3- and 0-dB broadside-coupled coupler and side-coupled coupler using alumina dielectric.

of parameters, namely, $b/2a$, ϵ_r, and s, the coupling length required in the case of a broadside-coupled image guide operating in the TM^y mode is considerably less than that required in the case of a side-coupled conventional image guide coupler operating in the TM^y mode.

Fig. 9 shows the comparison of characteristic of a nonradiative coupler and a side-coupled conventional image coupler for 3- and 0-dB couplings. Although the difference in coupling lengths in the two cases is small, the nonradiative coupler is expected to offer much smaller conductor loss, since the principal electric field is parallel to the metallic planes.

IV. Conclusion

The propagation parameters of a broadside-coupled dielectric image guide are analyzed using the mode-matching technique. For $\beta/\beta_o > 1$, the propagation corresponds to the image guide mode and the frequency at which $\beta/\beta_o = 1$ is the same irrespective of the spacing $2s$ between the dielectric strips in the case of the even mode. With the appropriate choice of the dielectric constant and dimensional parameters, the structure can operate as a nonradiative guide. The data presented on the even- and odd-mode propagation constants of the broadside-coupled image guide operating in the low-loss mode can be used in the design of couplers and filters at millimeter-wave frequencies.

Appendix

$$I_1(t) = \int_{p+b}^{2p+b} \cos\left[\beta_{1ym}\{y-(2p+b)\}\right] \cos\left(\frac{t\pi y}{2p+b}\right) dy$$

$$I_2(t) = \int_{p}^{p+b} \cos\left\{\beta_{2ym}(y-p)\right\} \cos\left(\frac{t\pi y}{2p+b}\right) dy$$

$$I_3(t) = \int_{p}^{p+b} \sin\left\{\beta_{2ym}(y-p)\right\} \cos\left(\frac{t\pi y}{2p+b}\right) dy$$

$$I_4(t) = \int_{0}^{p} \cos(\beta_{3ym} \cdot y) \cos\left(\frac{t\pi y}{2p+b}\right) dy$$

$$I_5(t) = \int_{p+b}^{2p+b} \sin\left[\beta_{1ym}\{y-(2p+b)\}\right] \sin\left(\frac{t\pi y}{2p+b}\right) dy$$

$$I_6(t) = \int_{p}^{p+b} \sin\left\{\beta_{2ym}(y-p)\right\} \sin\left(\frac{t\pi y}{2p+b}\right) dy$$

$$I_7(t) = \int_{p}^{p+b} \cos\left\{\beta_{2ym}(y-p)\right\} \sin\left(\frac{t\pi y}{2p+b}\right) dy$$

$$I_8(t) = \int_{0}^{p} \sin(\beta_{3ym} y) \sin\left(\frac{t\pi y}{2p+b}\right) dy$$

$$\bar{I}_1(t) = \int_{p+b}^{2p+b} \sin\left[\bar{\beta}_{1yn}\{y-(2p+b)\}\right] \sin\left(\frac{t\pi y}{2pb}\right) dy$$

$$\bar{I}_2(t) = \int_{p}^{p+b} \cos\left\{\bar{\beta}_{2yn}(y-p)\right\} \sin\left(\frac{t\pi y}{2p+b}\right) dy$$

$$\bar{I}_3(t) = \int_{p}^{p+b} \sin\left\{\bar{\beta}_{2yn}(y-p)\right\} \sin\left(\frac{t\pi y}{2p+b}\right) dy$$

$$\bar{I}_4(t) = \int_{0}^{p} \sin(\bar{\beta}_{3yn} y) \sin\left(\frac{t\pi y}{2p+b}\right) dy$$

$$\bar{I}_5(t) = \int_{p+b}^{2p+b} \cos\left[\bar{\beta}_{1yn}\{y-(2p+b)\}\right] \cos\left(\frac{t\pi y}{2p+b}\right) dy$$

$$\bar{I}_6(t) = \int_{p}^{p+b} \sin\left\{\bar{\beta}_{2yn}(y-p)\right\} \cos\left(\frac{t\pi y}{2p+b}\right) dy$$

$$\bar{I}_7(t) = \int_{p}^{p+b} \cos\left\{\bar{\beta}_{2yn}(y-p)\right\} \cos\left(\frac{t\pi y}{2p+b}\right) dy$$

$$\bar{I}_8(t) = \int_{0}^{p} \cos(\bar{\beta}_{3yn} y) \cos\left(\frac{t\pi y}{2p+b}\right) dy$$

$$E_t^{(1)} = E_t\left(\frac{2p+b}{2}\right)\cos(\beta_{4xt}s)$$

$$E_t^{(2)} = E_t\frac{t\pi}{2}\cos(\beta_{4xt}s)$$

$$E_t^{(3)} = E_t\beta_{4xt}\left(\frac{2p+b}{2}\right)\sin(\beta_{4xt}s)$$

$$E_t^{(4)} = E_t\left(\frac{2p+b}{2}\right)\sin(\beta_{4xt}s)$$

$$E_t^{(5)} = E_t\frac{t\pi}{2}\sin(\beta_{4xt}s)$$

$$E_t^{(6)} = E_t\beta_{4xt}\left(\frac{2p+b}{2}\right)\cos(\beta_{4xt}s)$$

$$B_m^{(1)} = B_m\cos(\beta_{xm}a) + B_m'\sin(\beta_{xm}a)$$

$$B_m^{(2)} = -B_m\sin(\beta_{xm}a) + B_m'\cos(\beta_{xm}a)$$

$$L_t^{(1)} = L_t\beta_{4xt}\left(\frac{2p+b}{2}\right)\cos(\beta_{4xt}s)$$

$$L_t^{(2)} = L_t\left(\frac{2p+b}{2}\right)\sin(\beta_{4xt}s)$$

$$L_t^{(3)} = L_t\frac{t\pi}{2}\sin(\beta_{4xt}s)$$

$$L_t^{(4)} = L_t\beta_{4xt}\left(\frac{2p+b}{2}\right)\sin(\beta_{4xt}s)$$

$$L_t^{(5)} = L_t\left(\frac{2p+b}{2}\right)\cos(\beta_{4xt}s)$$

$$L_t^{(6)} = L_t\left(\frac{t\pi}{2}\right)\cos(\beta_{4xt}s)$$

$$G_n^{(1)} = G_n\sin(\bar{\beta}_{xn}a) - G_n'\cos(\bar{\beta}_{xn}a)$$

$$G_n^{(2)} = G_n\cos(\bar{\beta}_{xn}a) + G_n'\sin(\bar{\beta}_{xn}a)$$

$$Q_m = \beta_{3ym}\epsilon_r\tan(\beta_{3ym}p)$$

$$R_m = \beta_{2ym}\cos(\beta_{2ym}b)$$

$$S_m = Q_m\sin(\beta_{2ym}b)$$

$$T_m = \beta_{2ym}\cos(\beta_{1ym}p)$$

$$P_m = \left[\frac{-\beta_{2ym}I_2(t) + Q_mI_3(t)}{-R_m + S_m}\right]\cos(\beta_{1ym}p)$$

$$U_m = I_1(t) + \frac{P_m}{\epsilon_r}$$

$$v_m = \frac{T_mI_4(t)}{(R_m - S_m)\cos(\beta_{3ym}p)}$$

$$W_m = U_m + V_m$$

$$X_m = \beta_{1ym}I_5(t) - \beta_{2ym}\left[\frac{\beta_{2ym}I_6(t) + Q_mI_7(t)}{-R_m + S_m}\right] \cdot \frac{\cos(\beta_{1ym}p)}{\epsilon_r}$$

$$Y_m = \frac{\beta_{3ym}T_mI_8(t)}{(R_m - S_m)\cos(\beta_{3ym}p)}$$

$$Z_m = X_m + Y_m$$

$$U_m^{(1)} = I_1(t) + P_m$$

$$W_m^{(1)} = U_m^{(1)} + V_m$$

$$\bar{Q}_n = \bar{\beta}_{3yn} \cot\left(\bar{\beta}_{3yn} p\right)$$

$$\bar{R}_n = \bar{\beta}_{2yn} \cos\left(\bar{\beta}_{2yn} b\right)$$

$$\bar{S}_n = \bar{Q}_n \sin\left(\bar{\beta}_{2yn} b\right)$$

$$\bar{T}_n = \bar{\beta}_{2yn} \sin\left(\bar{\beta}_{1yn} p\right)$$

$$\bar{P}_n = \frac{\beta_{2yn} I_2(t) + Q_n \bar{I}_3(t)}{\bar{R}_n + \bar{S}_n} \sin\left(\bar{\beta}_{1yn} p\right)$$

$$\bar{U}_n = \bar{I}_1(t) - \bar{P}_n$$

$$\bar{V}_n = \frac{\bar{T}_n \bar{I}_4(t)}{\left(\bar{R}_n + \bar{S}_n\right) \sin\left(\bar{\beta}_{3yn} p\right)}$$

$$\bar{W}_n = \bar{U}_n - \bar{V}_n$$

$$\bar{X}_n = \bar{\beta}_{1yn} \bar{I}_5(t) - \left[- \frac{\bar{\beta}_{2yn} \bar{I}_6(t) + \bar{Q}_n \bar{I}_7(t)}{\bar{R}_n + \bar{S}_n} \right] \sin\left(\bar{\beta}_{1yn} p\right)$$

$$\bar{Y}_n = \frac{\bar{\beta}_{3yn} \bar{T}_n \bar{I}_8(t)}{\left(\bar{R}_n + \bar{S}_n\right) \sin\left(\bar{\beta}_{3yn} p\right)}$$

$$\bar{Z}_n = \bar{X}_n - \bar{Y}_n$$

$$\alpha_t = \begin{cases} 1, & \text{if } t \neq 0 \\ 3, & \text{if } t = 0. \end{cases}$$

REFERENCES

[1] E. A. J. Marcatili, "Dielectric rectangular waveguide and directional coupler for integrated optics," *Bell Syst. Tech. J.*, vol. 48, pp. 2071–2102, Sept., 1969.

[2] R. M. Knox and P. P. Toulios, "Integrated circuits for the millimeter through optical frequency range," in *Proc. Symp. Submillimeter Waves* (New York, NY), Mar. 31–Apr. 2, 1970.

[3] R. M. Knox and P. P. Toulios, "A *V*-band receiver using image line integrated circuits," in *Proc. Nat. Electronics Conf.*, Oct. 16–18, 1974, Paper V 29, pp. 489–492.

[4] W. V. McLevige, T. Itoh, and R. Mittra, "New waveguide structure for millimeter wave and optical integrated circuits," *IEEE Trans. Microwave Theory Tech.*, vol. MTT-23, pp. 788–794, Oct. 1975.

[5] R. M. Knox, "Dielectric waveguide: A low cost option for IC's," *Microwaves*, vol. 15, pp. 56–57, Mar. 1976.

[6] R. Rudokas and T. Itoh, "Passive millimeter wave IC components made of inverted strip dielectric waveguides," *IEEE Trans. Microwave Theory Tech.*, vol. MTT-24, pp. 978–981, Dec. 1976.

[7] T. Itoh, "Inverted strip dielectric waveguide for millimeter wave integrated circuits," *IEEE Trans. Microwave Theory Tech.*, vol. MTT-24, pp. 821–827, Nov. 1976.

[8] T. Itoh and B. Adelseck, "Trapped image guide for millimeter wave circuits," *IEEE Trans. Microwave Theory Tech.*, vol. MTT-28, pp. 1433–1436, Dec. 1980.

[9] J. A. Paul and Y. W. Chang, "Millimeter wave image guide integrated passive devices," *IEEE Trans. Microwave Theory Tech.*, vol. MTT-26, pp. 751–754, Oct. 1978.

[10] T. Yoneyama and S. Nishida, "Nonradiative dielectric guide for millimeter wave integrated circuits," *IEEE Trans. Microwave Theory Tech.*, vol MTT-22, pp. 1188–1192, Nov. 1981.

[11] S. Shindo and T. Itanami, "Low-loss rectangular dielectric image line for millimeter-wave integrated circuits," *IEEE Trans. Microwave Theory Tech*, vol. MTT-26, pp. 747–751, Oct. 1978.

[12] K. Solbach and I. Wolff, "Electromagnetic fields and phase constants of dielectric image lines," *IEEE Trans. Microwave Theory Tech.*, vol. MTT-26, pp. 266–274, Apr. 1978.

[13] R. Mittra *et al.*, "Analysis of open dielectric wave guides using mode matching technique and variational method," *IEEE Trans. Microwave Theory Tech.*, vol. MTT-28, pp. 36–43, Jan. 1980.

[14] R. F. Harrington, *Time Harmonic Electromagnetic Fields*. New York: McGraw-Hill, 1961.

A Method of Avoiding the Edge Current Divergence in Perturbation Loss Calculations

LEONARD LEWIN, FELLOW, IEEE

Abstract—**From a consideration of the properties near the edge of a flat finite-thickness strip and an elliptic cross-section strip, it is shown that the divergence that arises in the perturbation method near a sharp edge can be handled by halting the loss calculation at a definite distance just short of the strip edge. This distance can be expressed in terms of the radius of curvature at the tip for a rounded edge, and in terms of the strip thickness for a flat edge.**

I. INTRODUCTION

A commonly used loss calculation method proceeds by taking the tangential magnetic field, as determined for the lossless case, calculating first the surface currents on the metal boundaries and then calculating the loss from these currents on the assumption that they are not affected substantially in form by the finite metal conductivity. The method can be applied if the metal thickness is everywhere sufficiently greater than the skin depth, and can even be used for infinitely thin strips or diaphragms when the very small amount of thickness that would be needed to appreciably exceed the skin depth would not alter the field substantially from the theoretical value in the ideal (zero-thickness) case. The one place where this cannot be done is for the axial current along a strip edge, since the ideal current density near the edge varies as $r^{-1/2}$, where r is the distance from the edge. For this variation, the needed square of the current density varies as $1/r$ and produces a logarithmic divergence if integrated to the strip edge at $r = 0$. Since all such strips, in practice, have a certain thickness, and often a slightly rounded edge, an examination of the local fields in such cases may be expected to show how to deal with the divergence.

One method of avoiding this divergence altogether is to simply assume a finite thickness and to carry out the usually much more involved analysis for the thick-strip case. This has been done by Cockroft [1] for isolated rectangular conductors, and by Kaden [2] for a microstrip configuration. The problem with this method is that it requires a *major* change in the field calculations just in order to accommodate a local feature in the immediate neighborhood of the edge. Nosich and Shestopalov [3], assuming a rounded edge of diameter equal to the strip thickness, noted that the magnetic field from a cylinder of radius w varies as $1/kw$, so that the actual field near the edge singularity should not become greater than this. They therefore stop the integration short by the requisite amount, of the order of $(kw)^2$, where $k = 2\pi/\lambda$. Not only is this truncation limit somewhat indefinite, but it is also frequency dependent, and assumes that the edge is rounded like a circular cylinder.

When the analysis for the nonzero thickness case is available, there is, in fact, no need to utilize the perturbation method at all; and Wheeler [4], using a technique based on an "incremental inductance" concept, showed how the losses could be calculated more directly. However, since the purpose of this paper is to be able to use the zero-thickness analysis, and to *avoid* extending it to the nonzero thickness case, it does not seem possible to adapt Wheeler's method for this purpose, since the needed normal derivative is not available.

Manuscript received May 11, 1983; revised February 7, 1984.

The author is with the Electromagnetics Laboratory, Department of Electrical and Computer Engineering, University of Colorado, Boulder, CO 80309.

0018-9480/84/0700-0717$01.00 ©1984 IEEE